Civil Engineering Dimension, Vol. 24, No. 1, March 2022, 1-10
ISSN 1410-9530 print / ISSN 1979-570X online
DOI: 10.9744/CED.24.1.1-10

Nonlinear Analysis of Reinforced Geopolymer Concrete Beams

Chong, K.[1], Suryanto, B.[1*], Tambusay, A.[1,2], and Suprobo, P.[2]

Abstract: To decarbonise the current construction sector and meet the global net-zero target, there is a pressing need to develop an environmentally friendly alternative to Portland cement concrete. Alkali activated and geopolymer concrete have much to offer in this regard. At present, however, there is limited study on the behaviours of alkali activated structural members, particularly on flexural members, which encompass most practical design situations. This paper presents a database of 37 tests on slender alkali activated and geopolymer concrete beams available in the literature, with the aim to investigate the flexural strengths of this alternative concrete when used as a structural member. In addition, the results of nonlinear finite element analyses on fourteen reinforced geopolymer concrete beams are presented to highlight key influencing factors governing the behaviour and failure of flexural members. Of particular interest is to study the influence of reinforcement ratio, compressive strength, and material brittleness on the overall strength and ductility. Overall, it is shown that the flexural response of geopolymer concrete beams under short-term loading is comparable to that of ordinary reinforced concrete beams.

Keywords: Alkali activated concrete; geopolymer concrete; beam, flexural failure; ATENA.

Introduction

Over the past few decades, significant advancements have been made towards understanding the properties and behaviour of alkali activated concrete (including those referred to as geopolymer concrete). Much research activity has focused on mix development and material characterisation [1-3], finding alternative activators and precursors [4-7], and optimum curing conditions [8]. These developments are well documented in various reports [9-11] and form the main themes for international conferences and research projects.

In comparison, a relatively limited number of studies have been reported describing the behaviour of structural members constructed with alkali activated or geopolymer concrete (in the latter, the binder is generally obtained through the synthesis of aluminosilicate source materials, e.g., low-calcium fly-ash or metakaolin [2,4-6,9]). Sumajouw and Rangan [12] investigated the behaviour of reinforced geopolymer concrete beams and columns and they reported that the test specimens exhibited similar crack pattern, load capacity and failure mode to conventional reinforced concrete members.

[1]Institute of Built Environment; Heriot-Watt University; Edinburgh; UNITED KINGDOM.
[2]Department of Civil Engineering, Faculty of Civil, Planning and Geo Engineering, Sepuluh Nopember Institute of Technology, Surabaya, INDONESIA.
*Corresponding author; Email: B.Suryanto@hw.ac.uk

Note: Discussion is expected before July, 1st 2022, and will be published in the "Civil Engineering Dimension", volume 24, number 2, September 2022.

Received 06 January 2022; revised 26 February 2022; accepted 23 March 2022

Moreover, the load capacities of the beams and columns were found to be in good agreement with predictions obtained using the design procedures developed originally for ordinary concrete. Yost *et al.* [13] conducted experimental testing on geopolymer concrete beams to investigate the load capacity and failure mode of a series of beams with differing reinforcement arrangements. They reported similar findings, although also found that geopolymer concrete tends to be more brittle than ordinary concrete. Overall, both studies concluded that this alternative concrete is a viable substitute for Portland cement concrete.

A more recent study by Monfardini and Minelli [14] demonstrated the full-scale application of geopolymer concrete by testing two large-scale reinforced concrete beams. A ductile response was observed from the two beams tested, with final failure governed by the tension reinforcement yielding followed by concrete crushing. More recently, Prinsse *et al.* [15] investigated the time-dependent behaviour of alkali activated slag and slag/fly-ash blended concrete at both material and structural levels. The results showed an apparent reduction of flexural and tensile splitting strength and elastic modulus with time. This was particularly evident in the blended slag/fly-ash mix and was attributed to the more significant moisture loss experienced by this particular mix. However, no significant differences were observed between the load capacities of the beams tested 1, 2 and 5 months after casting, indicating that the reduction in material properties did not exert a notable influence at the structural level.

In the abovementioned studies, attention has been directed primarily towards the response of alkali

activated and geopolymer structural members at the ultimate limit state, with a comparison of measured load capacities against the predictions of the design code of practice generally presented. However, only limited studies have been undertaken to establish a procedure that can predict the full load-deflection response of a structural member. The utilisation of a nonlinear finite element analysis software could be useful in this regard, as it can provide a base of knowledge for a wide range of parameters to be tested. This knowledge can be subsequently transferred to aid in designing and assessing reinforced alkali activated concrete structural elements.

In this paper, the nonlinear finite element software ATENA [16] is utilised to enable a detailed analysis of the effect of the primary influencing factors on the overall load-deflection response of alkali activated and geopolymer beams. Particular emphasis is placed on flexural behaviour because it forms the primary governing failure mechanism for most structural designs. A database of available experimental data in the literature is also presented to provide a better understanding of the flexural strengths of reinforced alkali activated and geopolymer concrete beams.

Test Data of Flexural Failures of Reinforced Alkali Activated and Geopolymer Concrete Beams

Table 1 presents the database of flexural failures of 37 reinforced alkali activated and geopolymer concrete beams from six different experimental studies available in the literature. This includes twelve beams tested by Sumajouw and Rangan [12]; six beams tested by Yost *et al.* [13]; two beams tested by Monfardini and Minelli [14]; five beams tested by Prinsse *et al.* [15], and twelve other beams tested by Du *et al.* [17]. Of these, 35 beams have shear links provided over the entire beam length, whilst the remaining two beams have shear links within the shear span only. The primary test variables include:

(i) Tensile reinforcement ratio ρ_s from 0.66% to 5.37% (of which over two-thirds is under 2.2%)
(iii) Concrete compressive strength f_c, ranging from 17 to 87 MPa
(iv) Yield strength of tensile reinforcement f_y in the range 450–580 MPa

Figure 1 presents the relationship between the tensile reinforcement ratio ρ_{st} (=A_{st}/bd) and the normalised

Table 1. Database of Alkali Activated and Geopolymer Reinforced Concrete Beams.

Ref	Beam Label	Dimensions	Tension Reinforcement				Compression Reinforcement					Shear Links		Concrete		Test Results		
		W × D × L (mm×mm×mm)	No–dia (mm)	A_{st} (mm²)	d_t (mm)	ρ_{st} (%)	f_{yt} (MPa)	No–dia (mm)	A_{sc} (mm²)	d_c (mm)	ρ_{sc} (%)	f_{yc} (MPa)	Spacing (mm)	f_{ys} (MPa)	f_c (MPa)	E (GPa)	P_u (kN)	d_{Pu} (mm)	FM
Sumajouw and Rangan [12]	GBI-1	200×300×3000	3–12	339	257	0.66	550	2–12	226	43	0.57	550	12–150	550	37	21	108.5	56.6	SY
	GBI-2	200×300×3000	3–16	603	255	1.18	560	2–12	226	43	0.57	550	12–150	550	42	22.5	171.2	46.0	SY
	GBI-3	200×300×3000	3–20	942	253	1.86	560	2–12	226	43	0.57	550	12–150	550	42	22.5	229.4	27.9	SY
	GBI-4	200×300×3000	3–24	1357	251	2.70	557	2–12	226	43	0.57	550	12–150	550	37	21	320.5	29.2	CC
	GBII-1	200×300×3000	3–12	339	257	0.66	550	2–12	226	43	0.57	550	12–150	550	46	23.5	111.1	54.3	SY
	GBII-2	200×300×3000	3–16	603	255	1.18	560	2–12	226	43	0.57	550	12–150	550	53	24.4	179.4	47.2	SY
	GBII-3	200×300×3000	3–20	942	253	1.86	560	2–12	226	43	0.57	550	12–150	550	53	24.4	239.1	30.5	SY
	GBII-4	200×300×3000	3–24	1357	251	2.70	557	2–12	226	43	0.57	550	12–150	550	46	23.5	331.0	27.5	CC
	GBIII-1	200×300×3000	3–12	339	257	0.66	550	2–12	226	43	0.57	550	12–150	550	72	28.6	130.4	73.9	SY
	GBIII-2	200×300×3000	3–16	603	255	1.18	560	2–12	226	43	0.57	550	12–150	550	76	27.9	185.9	40.9	SY
	GBIII-3	200×300×3000	3–20	942	253	1.86	560	2–12	226	43	0.57	550	12–150	550	76	27.9	250.5	35.5	SY
	GBIII-4	200×300×3000	3–24	1357	251	2.70	557	2–12	226	43	0.57	550	12–150	550	72	28.6	359.5	37.0	SY
Yost [13]	FAU-1	305×152×3200	3–16	594	119	1.64	475*	–	–	–	–	475*	–	–	52.2	29.1	23.7	–	SY
	FAU-2	305×152×3200	3–16	594	119	1.64	475*	–	–	–	–	475*	–	–	54.7	32.1	25.4	–	SY
	FAU-3	305×152×3200	3–16	594	119	1.64	475*	–	–	–	–	475*	–	–	54.4	30.6	25.8	–	SY
	FAO-1	305×152×3200	5–22	1940	116	5.49	475*	2–13	265.4	31.5	0.29	475*	13–152	404	52.4	–	73.5	–	CC
	FAO-2	305×152×3200	5–22	1940	116	5.49	475*	2–13	265.4	31.5	0.29	475*	13–152	404	56.5	–	70.8	–	CC
	FAO-3	305×152×3200	5–22	1940	116	5.49	475*	2–13	265.4	31.5	0.29	475*	13–152	404	56.9	–	75.8	–	CC
M [14]	AAC1	200×300×5000	2–16	402	260	0.77	546	2–12	226	38	0.44	546	8–75	546	29	24	95	131	SY
	AAC2	200×300×5000	2–16	402	260	0.77	546	2–12	226	38	0.44	546	8–75	546	35	25.2	92	90	SY
Prinsse [15]	S50	150×200×1900	3–8	151	165	0.61	550*	2–8	101	35	0.41	550*	8–135	550	75.1	–	67.4	32.5	SY
	S50	150×200×1900	3–8	151	165	0.61	550*	2–8	101	35	0.41	550*	8–135	550	77.1	–	58.8	35.2	CC
	S50	150×200×1900	3–8	151	165	0.61	550*	2–8	101	35	0.41	550*	8–135	550	83.7	–	69.7	40.7	–
	S100	150×200×1900	3–8	151	165	0.61	580*	2–8	101	35	0.41	580*	8–135	580	86.6	–	67.6	30.1	SY
	S100	150×200×1900	3–8	151	165	0.61	580*	2–8	101	35	0.41	580*	8–135	580	83.7	–	66.3	37.4	SY
Du [17]	30-0.66-4	200×400×3600	3–14	462	350	0.66	498	2–8	101	50	0.14	498	10–100	358	28.3	–	135.0	–	SY
	30-1.63-4	200×400×3600	3–22	1140	350	1.63	452	2–8	101	50	0.14	452	10–100	358	28.3	–	271.7	–	SY
	30-1.61-5	200×500×3600	5–19	1451	433	1.68	482	2–8	101	50	0.14	482	10–100	358	28.3	–	467.9	–	SY
	30-2.71-4	200×400×3600	5–22	1901	330	2.88	452	2–8	101	50	0.14	452	10–100	358	28.3	–	361.8	–	CC
	50-0.66-4	200×400×3600	3–14	462	350	0.66	498	2–8	101	50	0.14	498	10–100	358	44.4	–	125.2	–	SY
	50-1.63-4	200×400×3600	3–22	1140	350	1.63	452	2–8	101	50	0.14	452	10–100	358	44.4	–	289.8	–	SY
	50-1.61-5	200×500×3600	5–19	1451	433	1.68	482	2–8	101	50	0.16	482	10–100	358	44.4	–	465.2	–	SY
	50-2.71-4	200×400×3600	5–22	1901	330	2.88	452	2–8	101	50	0.14	452	10–100	358	44.4	–	417.6	–	CC
	70-0.66-4	200×400×3600	3–14	462	350	0.66	498	2–8	101	50	0.14	498	10–100	358	59.9	–	143.0	–	SY
	70-1.63-4	200×400×3600	3–22	1140	350	1.63	452	2–8	101	50	0.14	452	10–100	358	59.9	–	305.7	–	SY
	70-1.61-5	200×500×3600	5–19	1451	433	1.68	482	2–8	101	50	0.16	482	10–100	358	59.9	–	470.0	–	SY
	70-2.71-4	200×400×3600	5–22	1901	330	2.88	452	2–8	101	50	0.14	452	10–100	358	59.9	–	450.3	–	SY

Notes: FM: failure mode; SY: steel yielding; CC: concrete crushing. * assumed value; – not determined.

sectional moment resistance $M/(bd^2)$. The latter was multiplied by a factor of $550/f_{yt}$ to account for differences in yield strength of the steel reinforcement used in the different experiments. In this figure, A_{st} is the area of longitudinal tension reinforcement (mm²), b denotes the width of beam (mm), d is the effective depth of the beam (mm), f_{yt} represents the yield strength of tension reinforcement (MPa), and M is the maximum recorded moment in the experiment (calculated from the load reported in the original paper). The constant 550 represents the typical mean yield strength of steel reinforcement used in Europe, with a characteristic strength of 500 MPa. The normalised data with a constant value of 420 (grade 420 steel in ACI318-19[18]) are added for comparative purposes.

Figure 1 shows that $M/(bd^2)$ displays an almost linear relationship with ρ_{st} up to reinforcement ratios of ~2%, representing the most common range in practice. No significant difference is observed between the five datasets, as indicated by the relatively narrow range of values. This is not unexpected as the moment capacity of under-reinforced beams is governed by the yield strength of the longitudinal tensile reinforcement. Figure 1 also indicates that under the same range of reinforcement ratios, the compressive strength of the concrete exerts only a minor influence on the reported moment capacity of the beams. Consider, for example, the three beams tested by Sumajouw and Rangan at a reinforcement ratio of ~1.2% (GBII series). Increasing the compressive strength from 42 MPa to 76 MPa results in an average increase of moment capacity of less than 10%. Beyond this range of reinforcement ratios, the deviation from linearity is evident due to the increasing influence of the compressive strength of the concrete and the amount of compression reinforcement (if present). At a reinforcement ratio of ~2.7%, Du beams show a consistent increase in normalised moment capacity from approximately 12 to 15 N/mm². A similar trend is exhibited for Sumajouw and Rangan beams.

In this work, fourteen beams from two experimental studies: two beams tested by Monfardini and Minelli [14] and twelve other beams tested by Sumajouw and Rangan [12] were selected and analysed in greater depth to determine the full load-deflection response. Hereinafter, these beams are referred to as the MM and SR beams. The concrete and steel reinforcement properties were inputted following the values reported in the original articles. However, the influence of the curing method adopted in each study on the mechanical properties of the concrete in the beam is neglected (i.e., mechanical properties were inputted based on test samples).

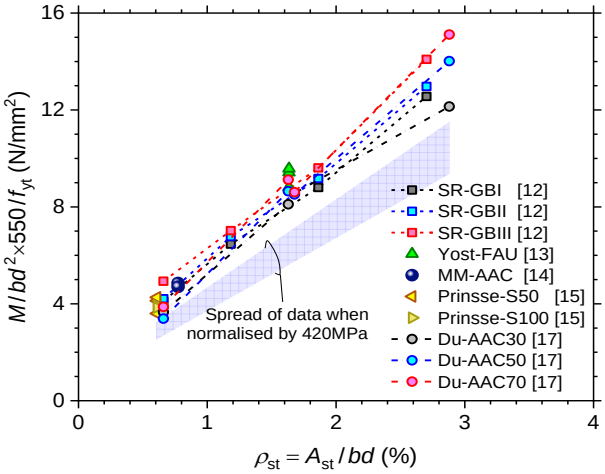

Figure 1. Normalised Sectional Moment Resistance of Reinforced Alkali Activated and Geopolymer Concrete Beams Plotted Against Reinforcement Ratio.

Monfardini and Minelli beams

Monfardini and Minelli tested two large-scale reinforced concrete beams to evaluate the structural performance of alkali activated, low-calcium fly-ash concrete [14]. Figure 2(a) displays the schematic of the beam geometry and reinforcement layout, together with the finite element mesh adopted in the analysis (detailed below) in Figure 2(b). The two beams were notionally identical and had overall dimensions of 200×300×5000mm, which is considered sufficiently large to provide a valuable set of data representative of a practical situation. Each beam had two 16mm bottom longitudinal bars, twenty-one 8mm closed shear links provided at 75mm spacing from each end of the beam, and two 12mm top reinforcement bars along the shear span of each beam. No shear links were provided at the central part of the beam to assess the ductility of the beam resulting from concrete crushing failure without the interference of shear links.

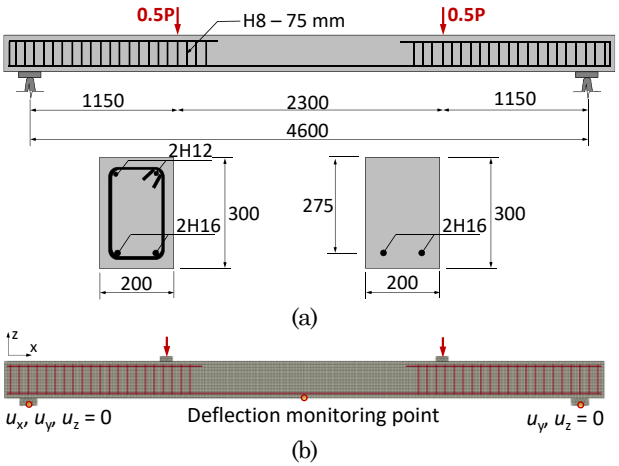

Figure 2. (a) Elevation and Cross-section Details of Monfardini and Minelli (MM) Beams [14]; (b) Typical Finite Element (FE) Mesh used in the Analysis. All dimensions in mm.

The compressive strengths of the concrete were 29MPa and 35MPa for beams MM1 and MM2, respectively. The mean yield and tensile strengths of the reinforcing bars were 545MPa and 649MPa, respectively, all corresponding to Italian grade B450C steel (denoted as H) [14].

Sumajouw and Rangan Beams

Sumajouw and Rangan [12] tested twelve reinforced fly-ash based geopolymer concrete beams to examine the influence of varying the compressive strength (from 37 to 76 MPa) and the longitudinal tensile reinforcement ratio (0.64% to 2.69%). Three series of four beams were tested in total, with the beams in each series differed mainly in the amount of bottom longitudinal reinforcement (3N12, 3N16, 3N20 and 3N24) covering a broad spectrum of reinforcement ratios from under to over reinforced section (see Fig. 3 and Table 2).

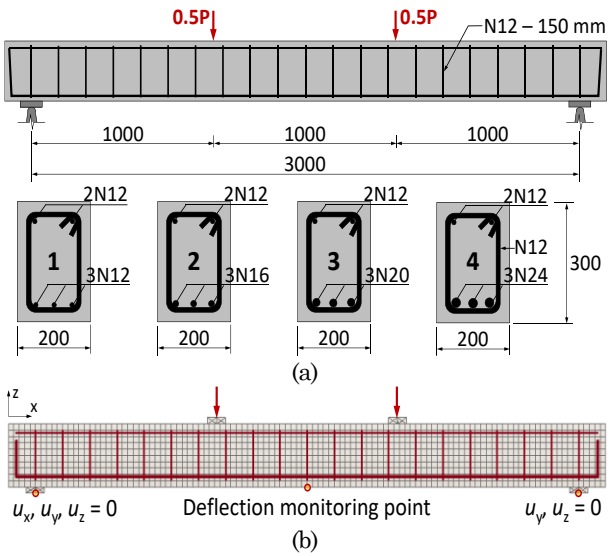

Figure 3. (a) Details of Sumajouw and Rangan (SR) beams [12]; (b) typical FE mesh used in the analysis. All dimensions in mm.

Table 2. Beam Reinforcement Details. All Beams Had Dimensions of 200×300×3300 mm [12].

Beam ID	Effective Depth (mm)	f_c' (MPa)	Reinforcement	
			Top	Bottom
GBI-1	257	37	2N12	3N12
GBI-2	255	42	2N12	3N16
GBI-3	253	42	2N12	3N20
GBI-4	251	37	2N12	3N24
GBII-1	257	46	2N12	3N12
GBII-2	255	53	2N12	3N16
GBII-3	253	53	2N12	3N20
GBII-4	251	46	2N12	3N24
GBIII-1	257	76	2N12	3N12
GBIII-2	255	72	2N12	3N16
GBIII-3	253	72	2N12	3N20
GBIII-4	251	76	2N12	3N24

Table 3. Steel Reinforcement Properties [12].

Diameter (mm)	Yield Strength (MPa)	Ultimate Strength (MPa)
12	550	680
16	560	690
20	560	675
24	557	660

In each beam, N12 shear links were provided at 150mm spacing. The variation in effective depth across the twelve beams is summarised in Table 2, together with the concrete compressive strengths reported in the original article. The properties of the steel reinforcement used in the experiment are presented in Table 3 [12].

Finite Element Analysis

The flexural responses of MM and SR beams were simulated using a nonlinear finite element (FE) analysis software ATENA Science [16]. Part of this program includes two fully integrated software packages, GiD and ATENA. GiD is an interactive pre-processor that enables the generation of FE model and relevant pertinent data such as material properties, loading and boundary conditions. Furthermore, GiD can be used to run an analysis, automatically transferring the FE model and respective data into ATENA Studio, which performs the analysis and provides post-processing capability with real-time visualisation during an analysis [19,20].

Figures 2(b) and 3(b) display typical FE models created in GiD for MM and SR beams, respectively. The concrete in each beam was modelled using 8-node hexahedral elements with a mesh size of 25mm for MM beams and 30mm for SR beams. The reinforcing bars were represented by truss elements and their bond to the surrounding concrete was modelled using the bond stress-slip relation recommended in CEB FIP MC1990 [21]. The slip at bond failure was taken as 0.6 mm, while the peak bond stresses were taken as $2\sqrt{f_c'}$ MPa [21].

The steel loading plates and supports were modelled using tetrahedral elements, with linear elastic property assigned to prevent localised yielding. Three monitoring points were established in each beam: one placed at the centre of each loading plate to monitor the reaction forces at the point of load application, and another placed at the underside of the beam at mid-span to monitor beam deflection. The loads measured at the two loading plates were added to obtain the total applied load.

In ATENA, the nonlinear behaviour of concrete is represented using fracture-plastic constitutive models [19,23]. The models are formulated based on a

decomposition of the total strain into elastic, plastic, and fracture components to deal with material damage and fractures within a continuum body. A brief description of the main constitutive models considered in this work is presented in this paper. For further details, the readers are referred to [19,23].

Constitutive Models

The constitutive model in ATENA is utilised to perform the nonlinear analysis. The formulation within the constitutive models implements the smeared crack approach, which refers to the distributed representation of concrete cracking. In this work, the fixed crack model was used. In this crack representation, the crack directions within each element are fixed based on the direction of the principal stresses at the onset of cracking (i.e., the direction of first cracking). Two new cracks may form at two other inclinations when the stresses govern. During loading, the direction of the principal stresses within each element may rotate and no longer coincide with the crack direction. Shear stresses may therefore develop on the cracked plane and result in shear slips; the use of a shear transfer model is therefore required.

Figures 4(a)-(c) display a graphical representation of the compression, tension and shear transfer models considered in this study [19,20,22,23]. In these models, stresses are computed from the strains in a local coordinate system following the crack orientation. The compression model implements the Menétry-William plasticity model [25], which is capable of representing the behaviour of concrete under multiaxial compressive loading. The failure surface is controlled by a hardening model, which is defined based on the response of concrete under uniaxial compression.

The ascending part after the elastic limit is determined using a hardening function, represented by the elliptical curve in Figure 4(a), as given by [19,20,23]:

$$\frac{\sigma_c}{f_c'} = f_{co} + (f_c' - f_{co})\sqrt{1 - \left(\frac{\varepsilon_c - \varepsilon_c^p}{\varepsilon_c}\right)^2} \quad (1)$$

$$\varepsilon_c^p = \frac{f_c'}{E_c} \quad (2)$$

$$E_c = (6000 - 15.5 f_{cu})\sqrt{f_{cu}} \quad (3)$$

$$f_{cu} = \frac{f_c'}{0.85} \quad (4)$$

where σ_c is the compressive stress (MPa); f_{co} is the compressive stress beyond the elastic limit and is taken as twice the concrete tensile strength (MPa); ε_c is the concrete strain (mm/mm); ε_c^p is the plastic strain at the peak stress (mm/mm); E_c is the concrete elastic modulus (MPa); and f_{cu} and f_c' are the cube and cylinder compressive strengths of the concrete.

Unlike the hardening part of the compression model, which is computed based on the strain, the softening part is computed based on the displacement, and the crush band approach is adopted to ensure mesh objectivity [23,24]. The post-peak compressive stress is assumed to decrease linearly from the peak to zero stress at a prescribed displacement w_d, as indicated by the descending linear curve in Figure 4(a).

The crush band size is taken as the FE size projected into the direction of the minimum compressive stress. The minimum band size is taken as the beam width to reduce the effects of mesh dependency [24]. The normalised compressive strength of the concrete is assumed to reduce linearly from 1.0 to 0.6 as the tensile strain perpendicular to the crack direction increases from 0.1% to 0.5% [20]. No further reduction in strength is considered beyond the transverse tensile strain value of 0.5%.

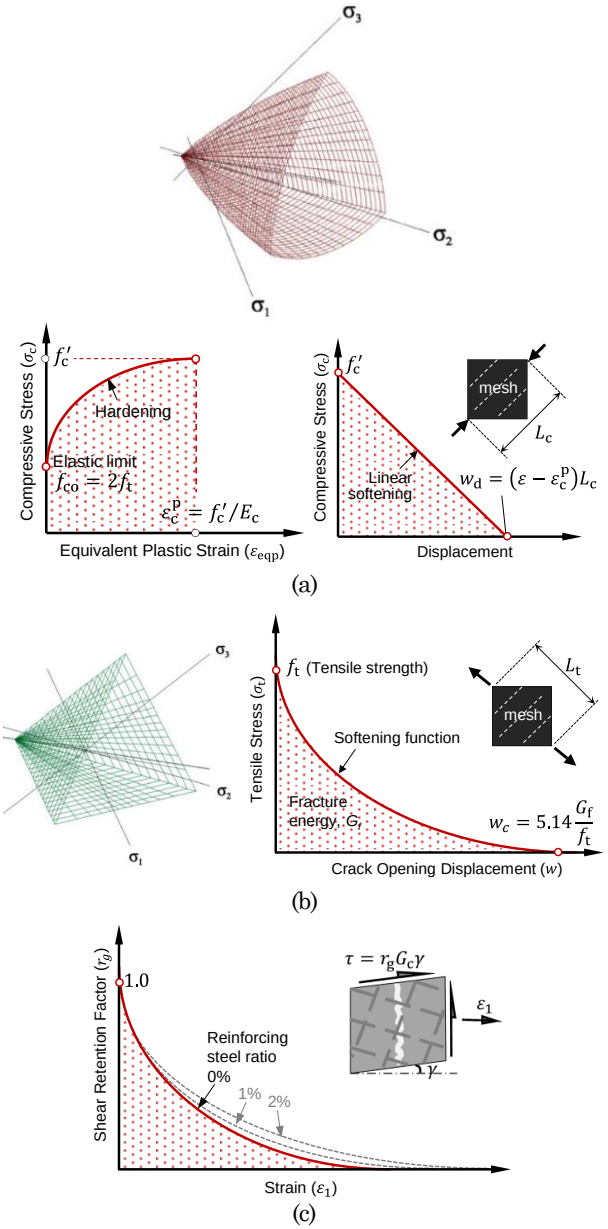

Figure 4. Constitutive Models for Concrete in ATENA: (a) Compression; (b) Tension; and (c) Shear Transfer Models [19,20,22,23].

In the fracture model, the Rankine failure criterion is used for defining concrete cracking. The tensile response of concrete after cracking is represented with an exponential softening function [20,24], with the tensile stress related to the crack opening displacement w and fracture energy G_f following the experimentally derived empirical expressions proposed by Hordijk [26]:

$$\frac{\sigma_t}{f_t} = \left[1 + \left(c_1 \frac{W}{w_c}\right)^3\right] e^{-c_2 \frac{W}{w_c}} - \frac{W}{w_c}(1 + {c_1}^3) e^{-c_2} \quad (5)$$

$$f_t = 0.24 {f_{cu}}^{\frac{2}{3}} \quad (6)$$

$$G_f = G_{f0} \left(\frac{f_c'}{10}\right)^{0.7} \quad (7)$$

$$w = \varepsilon_t L_t \quad (8)$$

where σ_t is the tensile stress (MPa); f_t is the concrete tensile strength (MPa); G_{f0} = 30N/m is the reference value of fracture energy based on the maximum aggregate size of 16mm [21]; w_c is the crack opening at the complete release of stress and is related to the concrete fracture energy (= $5.14 \frac{G_f}{f_t}$ mm); L_t is the characteristic length (mm) that relates the crack opening displacement w to the fracture strain ε_t following the crack band approach; c_1 and c_2 are empirical constants and taken as $c_1 = 3$ and $c_2 = 6.93$ [26]. The mesh orientation bias is minimised using an orientation correction factor [19,24].

To represent the reduction in the shear modulus of concrete after cracking, the model proposed by Kolmar [27] is adopted to determine the shear stiffness after cracking:

$$G = r_g G_c \quad (9)$$

$$r_g = c_3 \frac{-\ln\left(\frac{1000\varepsilon_1}{c_1}\right)}{c_2} \quad (10)$$

$$c_1 = 7 + 333(\rho - 0.005) \quad (11)$$

$$c_2 = 10 - 167(\rho - 0.005) \quad (12)$$

where G is the shear modulus after cracking (MPa); r_g is the shear retention factor; G_c is the initial shear modulus (MPa); ρ is the transformed ratio of steel reinforcement to the crack plane (taken as zero); c_1 and c_2 are parameters which are dependent on the steel bar(s) crossing the direction of the crack; and c_3 is a user scaling factor (=1 by default). The maximum shear stress that can be transmitted across a crack τ_{max} (MPa) follows the model proposed in [28]:

$$\tau_{max} = \frac{0.18\sqrt{f_c'}}{0.31 + \frac{24w}{a_g + 16}} \quad (13)$$

where w is the crack opening displacement (mm) and a_g is the maximum aggregate size (mm). For more details, readers are referred to reference [19,23].

In the analysis of MM beams, a parametric study was undertaken to establish the influence of the ductility of concrete in compression on the load-deflection response. The compression ductility softening parameter w_d, which represents material brittleness in compression, was varied from 0.5 to 2.5mm following the range of values proposed in previous experimental and numerical studies for ordinary concrete [20,24]. In the analysis of SR beams, w_d values were altered to best represent the increase in concrete brittleness with increasing compressive strength (see Table 5). The bottom longitudinal bars were extended to the ends of each beam and bent up, representing the actual bar configuration used in the experiment. For simplicity, the bond of reinforcing bars with the surrounding concrete was assumed to be in perfect condition (i.e., no bond-slip consideration). In all analyses, the load was applied as an incrementally imposed displacement until failure.

Table 4. Input Data for MM Beams.

Properties	MM1	MM2	Remark
f_c' (MPa)	29	35	Measured value
f_t (MPa)	2.52	2.86	Eq. 6
E_c (GPa)	31.9	34.4	Eq. 3
G_f (N/m)	55	63	Eq. 7
w_d (mm)	0.5-2.5	0.5-2.5	Assumed values
L_d (mm)	25	25	Chosen mesh size

Table 5. Input Data for Representative SR Beams.

Properties	GBI-1 GBI-4	GBI-2 GBI-3	GBII-1 GBII-4	GBIII-1 GBIII-4
f_c' (MPa)	37	42	46	76
f_t (MPa)	2.97	3.23	3.43	4.80
E_c (GPa)	35.1	36.8	38.0	43.6
G_f (N/m)	66	72	76	109
w_d (mm)	1.2	1.2	1.0	0.5
L_t (mm)	30	30	30	30

Results and Discussion

Monfardini and Minelli Beams

The predicted load-deflection response for Beams MM1 and MM2 is presented in Figures 5(a) and (b), with the failure crack patterns of Beams MM1 displayed in Figure 6 for illustrative purposes. It is apparent that the FE models can capture the initial response of the beams well. The occurrence of the first cracking and post-cracking response is well established, while the post-yielding response is overestimated, particularly around the transition to a plastic response where the most notable deviation is observed. This instance represents the local yielding of the bottom reinforcement at crack locations, and this overestimation may be attributed to lower values of yield strength than the reported values, in addition to a possible development of initial tensile stresses in the bars due to restrained shrinkage.

Comparing Figure 5(a) and (b), it is evident that Beam MM2 constructed with 35MPa concrete displayed a lower flexural resistance and ductility than Beam MM1 constructed with a slightly lower strength of concrete (29MPa). The plastic plateau region is shorter, which indicates a less ductile response. This might be attributed to the natural

variations within the material or other aspects that were unaccounted for during experimental testing. In addition, it should be noted that Beam MM2 was tested at a relatively early age (8 days) as opposed to 31 days for Beam MM1, which may contribute to the apparent difference in ductility as well.

Figures 5(a) and (b) also show that the overall member ductility is influenced by the ductility softening parameter w_d, which controls the post-peak compression softening (i.e., concrete brittleness in compression). As expected, the overall member ductility decreased as the concrete brittleness in compression increased. The experimental response lies comfortably with the w_d value of 2.0-2.5mm, whereas, for beam MM2, the respective w_d value is close to 1.0-1.5 mm. These represent the range of values that are established for ordinary concrete [24].

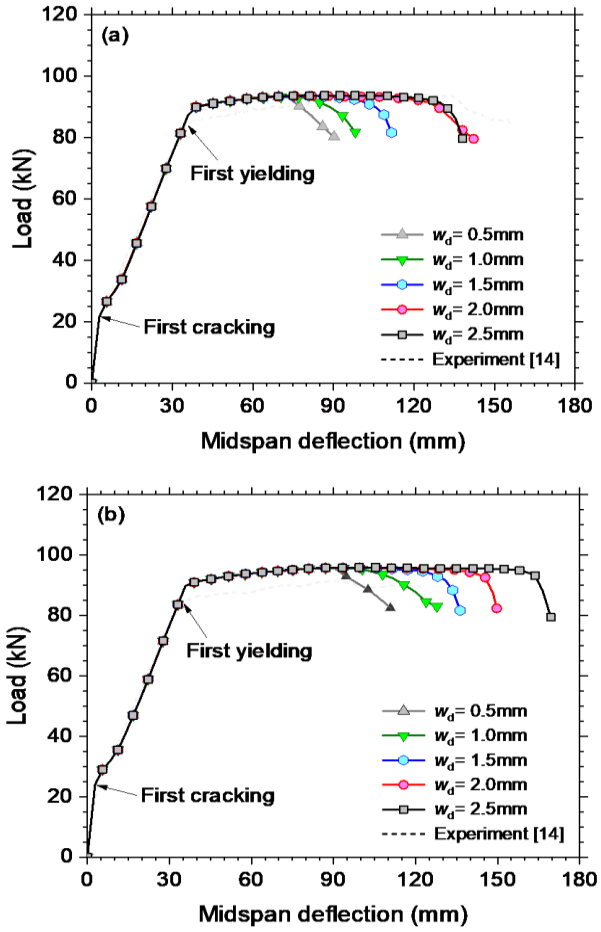

Figure 5. Predicted and Observed Load-deflection Response under Varying w_d Values for Beams (a) MM1 and (b) MM2.

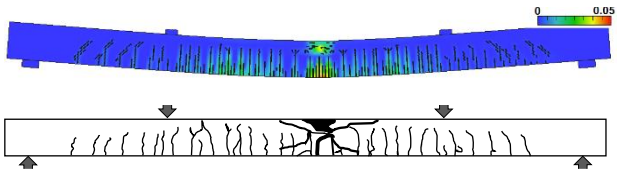

Figure 6. Comparison of Predicted and Observed Failure Crack Patterns of Beam MM1.

Sumajouw and Rangan Beams

The predicted and observed load-deflection responses for all SR beams are presented in Figures 7(a)-(c). As before, the solid lines represent the predicted responses, while the dashed lines denote the experimentally measured responses. In addition, a comparison of the predicted and observed failure crack patterns are displayed in Figure 9, while the comparison for the load and deflection capacities are presented in Tables 6 and 7.

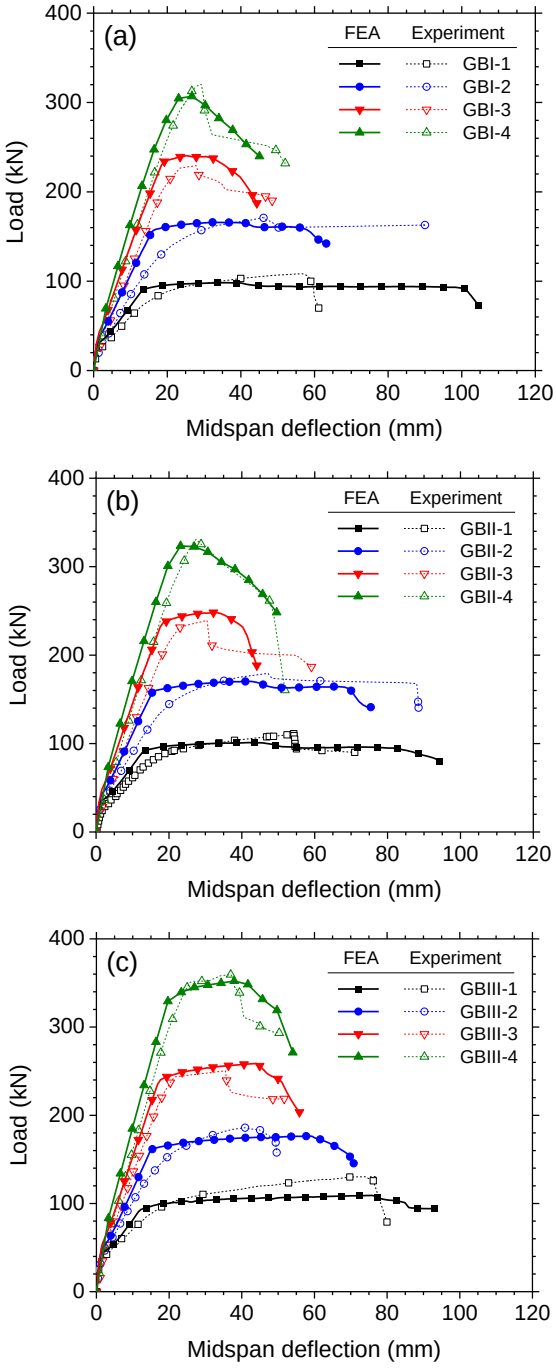

Figure 7. Comparison of Load-deflection Response for (a) GBI Series, (b) GBII Series, and (c) GBIII Series. Experimental Data from [12].

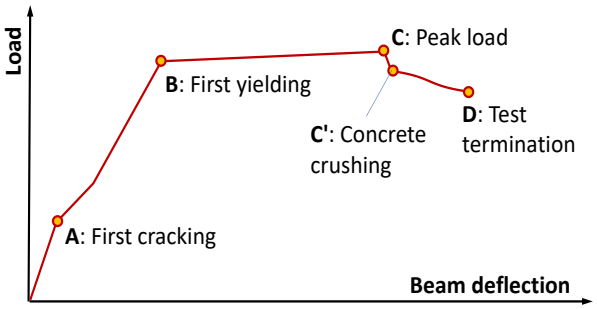

Figure 8. Schematic Diagram of an Idealised Load-deflection Response of a Reinforced Concrete Beam Tested under Point Loads [29].

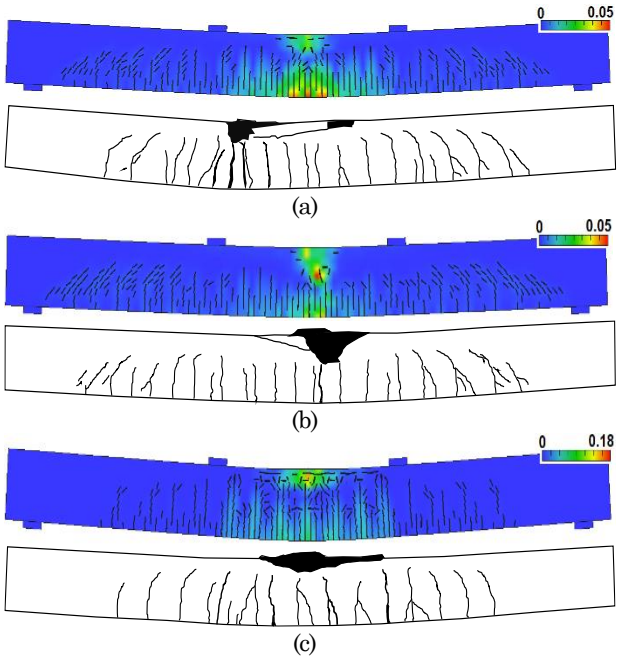

Figure 9. Comparison of Predicted and Observed Crack Patterns at Failure for GBI-2, GBI-3 and GBIII-1 Beams.

With reference to the schematic displayed in Figure 8, it can be inferred from Figure 7(a)-(c) that the increase in reinforcement ratio leads to a significant increase in the post-cracking stiffness (Section A-B) and the ultimate load capacity of the beams (Point C). As expected, geopolymer beams designed with low to intermediate reinforcement ratios ranging from 0.66% to 1.18% (denoted as GB-1 and GB-2) exhibit a ductile response due to extensive yielding of the bottom tensile longitudinal reinforcement (see Fig. 9(a)) [29]. Such a behavioural response would provide a considerable warning before failure ultimately occurs and is, therefore, aimed for in the design [31]. Within this range of reinforcement ratios, no discernible difference in load capacity is evident between beams constructed with different grades of concrete. Increasing the compressive strength almost two-fold from ~40MPa to 75MPa results in an increase in flexural strength of less than 10%.

The extent of the visible plateau region of the beams presented in Figures 7(a)-(c) is seen to be inversely related to the reinforcement ratio, with overall beam ductility decreasing with increasing reinforcement ratios. Accordingly, geopolymer beams designed with reinforcement ratios in the range of 1.86%-2.77% (GB-3 and GB-4 series) exhibit only a limited measure of ductility. In particular, Beams GBI-3, GBI-4, and GBII-4, exhibit no plateau region as failure is governed by crushing failure of the concrete in the compression zone before steel yielding (see Fig. 9(b)). In this instance, increasing the strength of the concrete is beneficial to increase the overall ductility, as indicated by the response of Beams GBIII-3 and GBIII-4 (see Fig. 7(c)). However, the increase in concrete strength also increases the brittleness, as indicated by the reduction in w_d values with increasing concrete strength (see Table 5). Overall, the predicted crack patterns are in good agreement with test observations (Figures 9(a)-(c)) and resemble well those of ordinary concrete beams [29,30].

The predicted and observed flexural capacities for all 12 beams investigated are presented in Table 6, together with the strength predictions using Eurocode 2 equations [32], based on the classical engineering beam theory (i.e., plane sections remain plane) and an equivalent rectangular stress block (all safety factors taken as 1.0). The ratio of the experiment-to-predicted strength ($\mathbf{P}_{u\text{-}Exp}/P_{u\text{-}FE}$) had a mean of 1.04 and a coefficient of variation (COV) of 6.5%, which is better than the ratio of the experiment-to-code predicted strength ($\mathbf{P}_{u\text{-}Exp}/P_{u\text{-}Cal}$) of 1.11 and a COV of 8.9%. As illustrated in Table 7, the predictions of the displacements at peak load were generally underestimated, but still within a reasonable range of accuracy, giving a mean of 1.09 and a COV of 21.8%.

Table 6. Summary of Predicted and Observed Load Capacities for All SR Beams.

Beam ID	$P_{u\text{-}Exp}$ (kN)	$P_{u\text{-}FE}$ (kN)	$P_{u\text{-}Calc}$ (kN)	Ratio	
				Exp/FE	Exp/Cal
GBI-1	108.5	98.3	90.7	1.10	1.20
GBI-2	171.2	165.9	156.4	1.03	1.09
GBI-3	229.4	239.5	231.8	0.96	0.99
GBI-4	320.5	307.0	303.2	1.04	1.06
GBII-1	111.1	101.1	92.6	1.10	1.20
GBII-2	179.4	170.3	159.5	1.05	1.12
GBII-3	239.1	248.2	237.5	0.96	1.01
GBII-4	331	323.5	315.4	1.02	1.05
GBIII-1	130.7	109.2	97.9	1.20	1.34
GBIII-2	185.9	176.4	163.7	1.05	1.14
GBIII-3	250.5	258.7	244.3	0.97	1.03
GBIII-4	359.5	352.2	336.8	1.02	1.07
			Mean	1.04	1.11
			COV%	6.50	8.90

Table 7. Summary of Predicted and Observed Midspan Deflection at Peak Load.

Beam ID	$d_{u\text{-}Exp}$ (mm)	$d_{u\text{-}FE}$ (mm)	Ratio Exp/FE
GBI-1	56.64	36.61	1.55
GBI-2	46.01	33.19	1.39
GBI-3	27.87	25.22	1.11
GBI-4	29.22	26.70	1.09
GBII-1	54.28	42.00	1.29
GBII-2	47.20	41.86	1.13
GBII-3	30.47	32.22	0.95
GBII-4	27.47	23.18	1.19
GBIII-1	73.93	75.80	0.98
GBIII-2	40.92	58.57	0.70
GBIII-3	35.50	44.04	0.81
GBIII-4	36.97	37.93	0.97
		Mean	1.09
		COV (%)	21.80

Concluding Remarks

The work presented highlights the application of nonlinear finite element analysis to critically assess the flexural behaviours of reinforced geopolymer concrete beams. Two experimental studies were simulated in ATENA to investigate the influence of various parameters on the overall load-deflection response and mode of failure. From the results presented, the following conclusions can be drawn:

(1) Nonlinear constitutive models developed originally for ordinary concrete can be used for simulating the nonlinear behaviour of geopolymer concrete members with sufficient accuracy.

(2) For the two large-scale reinforced geopolymer concrete beams, values of compression ductility parameter w_d (indicative of concrete brittleness in compression) were found within the range of values established for ordinary concrete.

(3) Concrete brittleness significantly influenced post-peak ductility of flexural members. As the ductility softening parameter w_d was increased from 0.5mm to 2.5mm, the overall member ductility almost doubled, whilst the load-carrying capacity remained relatively constant.

(4) In an under-reinforced beam, reinforcement ratio is shown to exert a more significant influence on the overall load capacity than compressive strength. For example, increasing the reinforcement ratio from approximately 0.7% to 1.2% (or almost double) results in an almost twofold increase in load capacity. On the other hand, increasing the compressive strength from 42 MPa to 72 MPa results in a marginal increase in load capacity (less than 10%). For such a beam (i.e., under-reinforced), ductile behaviour is expected due to the yielding of the reinforcement before concrete crushing.

(5) Geopolymer beams designed with moderate to high amounts of reinforcement (reinforcement ratios in the order of 2-3%) would exhibit a limited measure of ductility. This may lead to an undesirable brittle failure with little or no warning due to the crushing of the concrete in the compression zone before yielding of the steel reinforcement. Such a behavioural response must be avoided in design.

(6) When a full load-deflection analysis is not needed, as in many design circumstances, the graphical relationship between reinforcement ratio and normalised flexural capacity can be used to perform a quick calculation of flexural strength.

Part of the findings presented in this paper highlights the need for further investigations at an early age and over an extended period of time beyond the normal curing periods. Work in this direction is continuing.

Acknowledgements

The authors wish to thank both institutions for the facilities and support provided. This article was part of a dissertation submission of the first author.

References

1. Collins, F.G. and Sanjayan, J.G., Workability and Mechanical Properties of Alkali Activated Slag Concrete, *Cement and Concrete Research*, 29(3), 1999, pp. 455-458.
2. Hardjito, D., Wallah, S.E., Sumajouw, D.M., and Rangan, B.V., On the Development of Fly Ash-based Geopolymer Concrete, *ACI Materials Journal*, 101(6), 2004, pp. 467-472.
3. Xie, T., Visintin, P., Zhao, X., and Gravina, R., Mix Design and Mechanical Properties of Geopolymer and Alkali Activated Concrete: Review of the State-of-the-Art and the Development of a New Unified Approach, *Construction and Building Materials*, 256, 2020, p. 119380.
4. Ryu, G.S., Lee, Y.B., Koh, K.T., and Chung, Y.S., The Mechanical Properties of Fly Ash-based Geopolymer Concrete with Alkaline Activators, *Construction and Building Materials*, 47, 2013, pp. 409-418.
5. Lee, N.K. and Lee, H.K., Setting and Mechanical Properties of Alkali-activated Fly Ash/Slag Concrete Manufactured at Room Temperature, *Construction and Building Materials*, 47, 2013, pp. 1201-1209.
6. Nath, P. and Sarker, P.K., Flexural Strength and Elastic Modulus of Ambient-cured Blended Low-Calcium Fly Ash Geopolymer Concrete, *Construction and Building Materials*, 130, 2017, pp. 22-31.
7. Gao, X., Yu, Q.L., Lazaro, A., and Brouwers, H.J.H., Investigation on a Green Olivine Nano-Silica Source based Activator in Alkali Activated Slag-Fly Ash Blends: Reaction Kinetics, Gel

Structure and Carbon Footprint, *Cement and Concrete Research*, 100, 2017, pp. 129-139.
8. Topark-Ngarm, P., Chindaprasirt, P., and Sata, V., Setting Time, Strength, and Bond of High-Calcium Fly Ash Geopolymer Concrete, *Journal of Materials in Civil Engineering*, 27(7), 2015, p. 04014198.
9. RILEM TC 224-AAM, In: Provis, J.L. and Van Deventer, J.S., Editors, *Alkali Activated Materials: State-of-the-Art Report*, Springer Science & Business Media, 2013.
10. Ding, Y., Dai, J.G., and Shi, C.J., Mechanical Properties of Alkali-activated Concrete: A State-of-the-Art Review, *Construction and Building Materials*, 127, 2016, pp. 68-79.
11. Provis, J.L., Alkali-Activated Materials, *Cement and Concrete Research*, 114, 2018, pp. 40-48.
12. Sumajouw, M.D.J. and Rangan, B.V., Low-Calcium Fly Ash-based Geopolymer Concrete: Reinforced Beams and Columns, *Research Report GC3*, Curtin University of Technology, Australia, 2006, retrieved from https://espace.curtin.edu.au/handle/20.500.11937/23928
13. Yost, J.R., Radlińska, A., Ernst, S., Salera, M., and Martignetti, N.J., Structural Behavior of Alkali Activated Fly Ash Concrete. Part 2: Structural Testing and Experimental Findings, *Materials and Structures*, 46(3), 2013, pp. 449-462.
14. Monfardini, L. and Minelli, F., Experimental Study on Full-scale Beams made by Reinforced Alkali Activated Concrete Undergoing Flexure, *Materials*, 9(9), 2016, pp. 739.
15. Prinsse, S., Hordijk, D.A., Ye, G., Lagendijk, P., and Luković, M., Time-Dependent Material Properties and Reinforced Beams Behavior of Two Alkali-Activated Types of Concrete, *Structural Concrete*, 21(2), 2020, pp. 642-658.
16. ATENA, *Advanced Tool for Engineering Nonlinear Analysis*, available at www.cervenka.cz/products/atena/
17. Du, Y., Wang, J., Shi, C., Hwang, H.J., and Li, N., Flexural Behavior of Alkali-Activated Slag-based Concrete Beams, *Engineering Structures*, 229, 2021, p. 111644.
18. ACI 318-19, *Building Code Requirements for Structural Concrete*, American Concrete Institute, 2020.
19. Červenka, V., Jendele, L., and Červenka, J., *ATENA Program Documentation–Part 1: Theory*, Červenka Consulting, Prague, 2018.
20. Tambusay, A., Suprobo, P., Suryanto, B., and Don, W., Application of Nonlinear Finite Element Analysis on Shear-Critical Reinforced Concrete Beams, *Journal of Engineering & Technological Sciences*, 53(4), 2021, pp. 210408.
21. CEB-FIP Model Code 1990, *Design Code*, Comité Euro-International du Béton, 1993.
22. Don, W., Suryanto, B., Tambusay, A., and Suprobo, P., Forensic Assessments of the Influence of Reinforcement Detailing in Reinforced Concrete Half-Joints: A Nonlinear Finite Element Study, *Structures*, 38, 2022, pp. 689-703.
23. Červenka, J. and Papanikolaou, V.K., Three Dimensional Combined Fracture–Plastic Material Model for Concrete, *International Journal of Plasticity*, 24(12), 2008, pp. 2192-2220.
24. Červenka, J., Červenka, V., and Laserna, S., On Crack Band Model in Finite Element Analysis of Concrete Fracture in Engineering Practice, *Engineering Fracture Mechanics*, 197, 2018, pp. 27-47.
25. Menetrey, P. and Willam, K.J., Triaxial Failure Criterion for Concrete and its Generalization, *ACI Structural Journal*, 92(3), 1995, pp. 311-318.
26. Hordijk, D.A., *Local Approach to Fatigue of Concrete*, Ph.D Thesis, Delft University of Technology, 1991.
27. Kolmar, W., *Beschreibung der Kraftuebertragung Über Risse in Nichtlinearen Finite-Element-Berechnungen von Stahlbetontragwerken*, PhD Thesis, Darmstadt University of Technology, Germany, 1986.
28. Vecchio, F.J. and Collins, M.P., The Modified Compression-Field Theory for Reinforced Concrete Elements Subjected to Shear, *ACI Journal*, 83(2), 1986, pp. 219-231.
29. Tambusay, A., Suryanto, B., and Suprobo, P., Digital Image Correlation for Cement-based Materials and Structural Concrete Testing, *Civil Engineering Dimension*, 22(1), 2020, pp. 6-12.
30. Suryanto, B., Tambusay, A., and Suprobo, P., Crack Mapping on Shear-Critical Reinforced Concrete Beams using an Open Source Digital Image Correlation Software, *Civil Engineering Dimension*, 19(2), 2017, pp. 93-98.
31. Don, W., Chong, K., Aitken, M., Tambusay, A., Suryanto, B., and Suprobo, P., Influence of Link Spacing on Concrete Shear Capacity: Experimental Investigations and Finite Element Studies. *IOP Conference Series: Materials Science and Engineering*, 930(1), 2020, pp. 012052.
32. BS EN 1992-1-1:2004+A1:2014, *Eurocode 2: Design of concrete structures. General rules and rules for buildings*, British Standards Institution, 2004.